International Journal of Automotive Technology, Vol. 21, No. 2, pp. 397–406 (2020)
DOI 10.1007/s12239–020–0037–4

pISSN 1229–9138/ eISSN 1976–3832

REAL-FLUID MODELING FOR TURBULENT MIXING PROCESSES OF N-DODECANE SPRAY JET UNDER SUPERCIRITICAL PRESSURE

Kiyoung Jung[1)], Yongmo Kim[1)] and Namsu Kim[2)*]

[1)]School of Mechanical Engineering, Hanyang University, Seoul 04763, Korea
[2)]Advanced Combustion Laboratory, Korea Institute of Energy Research, 152 Gajeong-ro, Yuseong-gu, Daejeon 34129, Korea

(Received 28 December 2018; Revised 12 April 2019; Accepted 25 June 2019)

ABSTRACT–The multi-environment probability density function (MEPDF) approach using the real-fluid Equation of State (EoS) has been developed to numerically investigate the physical processes of the non-cryogenic n-dodecane fuel spray jet under the supercritical pressure. The MEPDF approach together with the conserved scalar formulation and the real-fluid library is utilized to account for the scalar fluctuation effects on the turbulent mixing processes of real fluids over the transcritical and supercritical spray conditions. To correctly predict the highly non-linear thermodynamic properties over a wide range of pressures and temperatures, this approach has adopted the RK-PR equations of state and dense-fluid correction models. In order to realistically and efficiently predict the supercritical spray jet with the strong anisotropic turbulence, the present study has adopted the RANS-based v^2–f model and the LES-based turbulence model. Simulations are made for the "Spray-A" benchmark case in the Engine Combustion Network. Based on numerical results, the detailed discussions are also made for the prediction capability of RANS/LES based real-fluid approach as well as the essential features of the real-fluid n-dodecane jet under the supercritical pressure.

KEY WORDS : Diesel spray, Supercritical pressure, Real-fluid modeling, MEPDF approach

1. INTRODUCTION

The elevated pressure has essentially led to increase the thermal efficiency and the power output in internal combustion engines such as rockets, gas turbines, and compression ignition engines. In the high-performance engines, the elevation of pressure eventually creates the supercritical flow. In the supercritical state, the surface tension almost disappears and the solubility approaches that of a gas. Moreover, the disappearance of the surface tension eventually results in widening the gas-liquid interfacial diffusion layer. These real-fluid properties are characterized by pressure-dependent solubility, gas-like diffusivity and liquid-like densities. Under supercritical pressure, these real-fluid characteristics are appeared for the cryogenic liquids as well as the non-cryogenic liquids. Especially in the kerosene/LOx liquid propellant rocket engines operated under supercritical pressure, the cryogenic liquid oxygen is used as oxidizer and the non-cryogenic kerosene is utilized as a fuel. Thus, it is quite desirable to develop the real-fluid models for the reliable prediction of cryogenic and non-cryogenic liquid flows at supercritical state.

For the cryogenic liquids, there were extensive experimental (Grisch *et al*., 2003; Gurliat *et al*., 2003; Oschwald *et al*., 2006) and numerical (Kim *et al*., 2011, 2012, 2013) works for injection dynamics and turbulent mixing/reacting processes under the supercritical pressure. The experimental results indicated that, under supercritical conditions, the non-cryogenic hydrocarbon liquid fuel sprays (Pickett *et al*., 2011; Falgout *et al*., 2015; ECN, 2015) and cryogenic liquid sprays have no clear interphase boundaries. The supercritical combustion of cryogenic and non-cryogenic liquid is dominantly controlled by turbulent diffusion process with real-fluid characteristics and extremely high gradients of thermodynamic properties. According to the experimental findings, the cryogenic liquid flows under supercritical pressures were successfully simulated by the single-phase real-fluid model (Kim *et al*., 2011, 2012). Recently, the systematic experimental studies (Falgout *et al*., 2015) have been conducted for the real-fluid fuel spray jets in a diesel-like supercritical environment. Especially, the "Spray-A" series performed in Engine Combustion Network (ECN, 2015) has been popularly adopted as a benchmark case especially in context with the multi-phase flow approaches (Pei *et al*., 2015; Wehrfritz *et al*., 2016; Kim *et al*., 2018). On the other hand, the recent studies (Ruiz *et al*., 2015; Ma and Ihme, 2017) revealed the insightful physics for Diesel injection processes at the supercritical pressures. Their studies for the gas–liquid interfacial structure quantified under what conditions two-phase spray dynamics transition to

**Corresponding author*. e-mail: nskim@kier.re.kr

diffusion dominated mixing. Ruiz *et al*. (2015) performed a large-eddy simulation (LES) using a real-fluid state equation to analyze the details of the transient mixing and the processes for the ECN Spray A target case (Pickett *et al*., 2011; Falgout *et al*., 2015). Their numerical results revealed the dominant effects of supercritical real-fluid effects on the instantaneous turbulent mixing processes. It was identified that the large density ratio between the supercritical fuel and the ambient gas leads to significant penetration of the jet with enhanced turbulent mixing at the tip and strong entrainment effects. Ma and Ihme (2017) carried out another LES simulation for the ECN spray jet. Their numerical results are qualitatively in good agreement with the experimental images even if the spreading angle of the fuel jet was considerably underestimated at the vicinity of the nozzle. However, the LES-based real-fluid modeling still requires the excessive CPU time especially for the complex real engines with the numerous injectors. Thus, especially for simulating the supercritical liquid flows in the practical complex high-pressure combustion systems, the RANS-based real-fluid model could be still a practical choice between accuracy and economy. So far, the RANS-based model has been applied to cryogenic mixing and reacting flow in supercritical pressure (Kim *et al*., 2011, 2012) rather than non-cryogenic diesel-fuel jets.

In this regard, this study has been mainly motivated to evaluate the capability of the RANS-based model and the LES-based approach for the simulation of the turbulent non-cryogenic fuel jets under the supercritical pressure. In the present study, the multi-environment probability density function approach using the real-fluid EoS has been applied to numerically investigate the physical processes of the non-cryogenic n-dodecane ECN Spray-A (Pickett *et al*., 2011; Falgout *et al*., 2015) under the supercritical pressure. Based on numerical results, the detailed discussions are also made for the prediction capability of RANS/LES based real-fluid approach as well as the essential features of the real-fluid n-dodecane jet under the supercritical pressure.

2. NUMERICAL METHOD

In the present study, the MEPDF approach together with the conserved scalar formulation and the real-fluid library has been developed to numerically investigate the supercritical turbulent spray mixing processes encountered in the diesel engines. The related models and formulations are described below

2.1. Real Fluid Equation of State

Due to the simplicity and robustness, the real-fluid modeling usually employs the two-parameter cubic EoS including Soave–Redlich–Kwong (SRK) EoS (Soave, 1972) and Peng–Robinson (PR) EoS (Peng and Robinson, 1976). However, according to Cismondi and Mollerup (2005), the two-parameter cubic EoS has the limited accuracy due to the inconsistency in the density dependence. To overcome this inconsistency, they proposed the following three-parameter cubic EOS including additional parameter δ_1.

$$p = \frac{\rho R_u T}{M_w - b\rho} - \frac{a\alpha(T)\rho^2}{(M_w + \delta_1 b\rho)(M_w + \delta_2 b\rho)} \tag{1}$$

Here, δ_2 is defined by $(1-\delta_1)/(1+\delta_1)$. Using this generalized cubic EoS, Kim *et al*. (2012) derived a formula for the thermodynamic properties of the mixture for use in combustion simulations of liquid rocket engines. It was confirmed that three-parameter cubic EoS is superior to the PR and SRK model in dealing with the fluid mixtures with different critical properties over various pressure and temperature ranges.

Definition of each parameter and constant value is given in the previous work of Kim *et al*. (2012). δ_1 of generalized cubic Eos is determined by the critical compressibility factor of fluid Z_c and original parameters $a\alpha$ and b are expressed as the function of additional parameter δ_1. If δ_1 is unity, Equation (1) becomes identical to that of original SRK and the other hand, if δ_1 is $1+\sqrt{2}$, it has the same formula as original PR. This implies that SRK and PR EoS are special cases of the RK-PR EoS with a specific value of Z_c. In order to consider the multi-component mixture fluids, the mixture is regarded as a unique pure hypothetical fluid with parameters needed in Equation (1) are obtained through the mixing rules. The variables $a\alpha_{mix}$ and b_{mix} used in the cubic-EoS of the mixture base are obtained through the mixing rule in the variables of the chemical species as follows.

$$a\alpha_{mix} = \sum_{i=1}^{N_s}\sum_{j=1}^{N_s} X_i X_j \sqrt{a_i a_j \alpha_i \alpha_j}(1-\bar{\kappa}_{ij}) \tag{2}$$

$$b = \sum_{i=1}^{N_s} X_i b_i \tag{3}$$

Here, X_i is the mole fraction of each species i, and $\bar{\kappa}_{ij}$ is the binary interaction coefficient. The first partial differential terms of $a\alpha_{mix}$ for T are derived,

$$\frac{\partial a_{ij}\alpha_{ij}}{\partial T} = \sqrt{a_i a_j}\left(\frac{1}{2}\sqrt{\frac{\alpha_i}{\alpha_j}}\frac{\partial \alpha_j}{\partial T} + \frac{1}{2}\sqrt{\frac{\alpha_j}{\alpha_i}}\frac{\partial \alpha_i}{\partial T}\right) - \frac{1}{4}\sqrt{\frac{\alpha_j}{\alpha_i^3}}\left(\frac{\partial \alpha_j}{\partial T}\right)^2 + \frac{1}{2}\sqrt{\frac{\alpha_i}{\alpha_j}}\frac{\partial^2 \alpha_j}{\partial T^2} + \frac{1}{2}\sqrt{\frac{\alpha_j}{\alpha_i}}\frac{\partial^2 \alpha_i}{\partial T^2}\Bigg] \tag{4}$$

2.2. Real Fluid Properties

According to the procedure of Kim *et al*. (2012), the related thermal properties such as isobaric specific heat, enthalpy and internal energy are calculated with utilizing basic fundamental thermodynamic relations. All properties first precomputed in an ideal state consider the dense fluid correction to ideal values to account for high pressure effects.

$$C_p(T,\rho) = C_{p0}(T) - \int_{\rho_0}^{\rho}\left[\frac{T}{\rho^2}\left(\frac{\partial^2 p}{\partial T^2}\right)_\rho\right]_T d\rho + \frac{T}{\rho^2}\left(\frac{\partial^2 p}{\partial T^2}\right)_\rho \Big/ \left(\frac{\partial p}{\partial \rho}\right)_T \quad (5)$$

$$e(T,p) = e_0(T) + \int_{\rho_0}^{\rho}\left[\frac{p}{\rho^2} - \frac{T}{\rho^2}\left(\frac{\partial p}{\partial T}\right)_\rho\right]_T d\rho \quad (6)$$

$$s(T,\rho) = s_0(T,\rho_0) + \int_{\rho_0}^{\rho}\left[\frac{1}{\rho^2}\left(\frac{\partial p}{\partial T}\right)_\rho\right]_T d\rho \quad (7)$$

The subscript '0' represents the calculated by ideal state assumption. The dense fluid correction terms in Equations (5) ~ (7) are determined using real fluid EoS. Transport property anomalies related to real fluid behaviors were reviewed by Congiunti *et al*. (2003). The transport property models under supercritical pressure are based on the Chapman–Enskog theory or the corresponding state theory. The model of viscosities in supercritical or transcritical region is derived by Chung *et al*. (1988). On the other hand, due to the lack of general theory, the mixture mass diffusion coefficientes at high pressure are evaluated by the empirical formula proposed by Takahashi (1975).

$$D_{ij}^{+} = \frac{0.00143T^{1.75}}{pM_{w,ij}^{1/2}\left[\left(\sum\nu\right)_i^{1/3} + \left(\sum\nu\right)_j^{1/3}\right]^2} \quad (8)$$

$$\frac{D_{ij}p}{(D_{ij}p)^{+}} = f(T_r, p_r) \quad (9)$$

$(D_{ij}p)^{+}$ denotes the value at low pressure (atmospheric pressure) and both of $T_r = T/T_c$ and $p_r = p/p_c$ are the temperature and pressure normalized by the critical values, respectively. Here, $f(T_r, p_r)$ is interpolated using Takahashi correlation according to T_r and p_r.

2.3. RANS-based v^2–f Turbulence Model

The v^2–f model proposed by Durbin *et al*. (1995) is used in this study. In addition to the turbulent kinetic energy and its dissipation rate in the standard $k-\varepsilon$ turbulence model, the wall-normal velocity fluctuation v^2 and its source term f are introduced as variables to incorporate near-wall turbulence anisotropy as well as non-local pressure-strain effects. In the real-fluid supercritical spray jet, the turbulent mixing process between the liquid jet and the ambient gas is highly influenced by the high gradients of thermophysical properties and the pseudo boiling process at the edge of real-fluid jet. Especially, the pseudo boiling results in thickening the real-fluid shear layer which possibly leads to the highly anisotropic turbulence structure. Thus, to consider the non-isotropic turbulence, it is expected that the v^2–f model has the much better prediction capability compared to the $k-\varepsilon$ model. It was also reported that the v^2–f model shows better predictive ability in many engineering problems than the conventional $k-\varepsilon$ turbulence models (Wu and Durbin, 1999; Cokljat *et al*., 2003).

In the v^2–f model, three transport equations (k, ε, and v^2) and one elliptic relaxation equation (f) are written below.

Table 1. Constants and definitions used in v^2–f turbulence model.

C_μ	0.22	C_1	1.4
$C_{\varepsilon 2}$	1.9	C_2	0.3
σ_k	1	C_L	0.23
σ_ε	1.3	C_η	70
T	$\max\{k/\varepsilon,\ 6(\nu/\varepsilon)^{1/2}\}$		
L	$C_L\ \max\{k^{3/2}/\varepsilon,\ C_\eta(\nu^3/\varepsilon)^{1/4}\}$		
$C_{\varepsilon 1}$	$C_{\varepsilon 1} = 1.4(1 + 0.05(k/\overline{v^2})^{1/2})$		

$$\frac{\partial(\bar\rho k)}{\partial t} + \nabla\cdot(\bar\rho\tilde{\mathbf{u}}k) - \nabla\cdot\left(\mu + \frac{\mu_t}{\sigma_k}\nabla k\right) = P_k - \varepsilon \quad (10)$$

$$\frac{\partial(\bar\rho\varepsilon)}{\partial t} + \nabla\cdot(\bar\rho\tilde{\mathbf{u}}\varepsilon) - \nabla\cdot\left(\mu + \frac{\mu_t}{\sigma_\varepsilon}\nabla\varepsilon\right) = \frac{C_{\varepsilon 1}P_k - C_{\varepsilon 2}\varepsilon}{\tau} \quad (11)$$

$$\frac{\partial\left(\bar\rho\overline{v^2}\right)}{\partial t} + \nabla\cdot\left(\bar\rho\tilde{\mathbf{u}}\overline{v^2}\right) - \nabla\cdot\left(\mu + \frac{\mu_t}{\sigma_k}\nabla\overline{v^2}\right) + kf - 6\frac{\overline{v^2}}{k}\varepsilon \quad (12)$$

$$L^2\nabla^2(f) - f = \frac{1}{\tau}\left[(C_1 - 6)\frac{\overline{v^2}}{\tilde k} - \frac{2}{3}(C_1 - 1)\right] - C_2\frac{P_k}{\tilde k} \quad (13)$$

In the v^2–f turbulence model, the turbulent viscosity is expressed as,

$$\mu_t = \rho f_\mu C_\mu \overline{v^2}\tau \quad (14)$$

Here, P_k is the production rate of turbulent energy and defined by $P_k = \rho u_i' u_j' \partial u_i/\partial x_j$. The related parameters and the semi-empirical model constants are listed in Table 1. τ and L are the turbulent time scale and the turbulent length scale, respectively.

2.4. LES Model

Unlike the RANS-based turbulence model, the LES approach directly resolves the large-scale turbulent flow and models the subgrid-scale unresolved flows. The LES equations for the resolved fields can be derived applying a low pass filter.

$$\frac{\partial\bar\rho}{\partial t} + \frac{\partial\bar\rho\tilde u_j}{\partial x_j} = 0 \quad (15)$$

$$\frac{\partial\bar\rho\tilde u_i}{\partial t} + \frac{\partial\bar\rho\tilde u_i\tilde u_j}{\partial x_j} = -\frac{\partial\bar p}{\partial x_i} + \frac{\partial}{\partial x_j}\left(2\mu_{eff}\left(\tilde S_{ij} - \frac{1}{3}\tilde S_{kk}\delta_{ij}\right)\right) \quad (16)$$

$$\frac{\partial\bar\rho\tilde\phi_k}{\partial t} + \frac{\partial\bar\rho\tilde u_j\tilde\phi_k}{\partial x_j} = \frac{\partial}{\partial x_j}\left((D + D_t)\frac{\partial\tilde\phi_k}{\partial x_j}\right) + \tilde\omega_k \quad (17)$$

Where the bar indicates the low-pass filtered quanties, the tilde indicates the Favre-filtered quantities, $\bar\rho$ is the filtered density, $\tilde u_i$ is the filtered velocity vector

component, $\bar{p}$ is the filtered pressure, μ is the laminar viscoity, and μ_t is the eddy viscosity. $\tilde{S}_{ij}$, the filtered rate of strain is defined by

$$\tilde{S}_{ij} = \frac{1}{2}\left(\frac{\partial \tilde{u}_i}{\partial x_j} + \frac{\partial \tilde{u}_j}{\partial x_i}\right) \tag{18}$$

Here, $\tilde{\phi}_k$ represents filtered transported scalar quantities, D is the molecular diffusivity and D_t is the turbulent diffusivity, and $\overline{\omega}_k$ is the filtered reaction source term of scalar k. The eddy viscosity is modeled by the Vreman model (Vreman, 2004). Vreman proposed the following model for the subgrid-scale (SGS) viscosity:

$$\mu_t = c_v \bar{\rho}\sqrt{B_\beta / (\alpha_{ij}\alpha_{ij})} \tag{19}$$

with

$$B_\beta = \beta_{11}\beta_{22} + \beta_{11}\beta_{33} + \beta_{22}\beta_{33} - \beta_{12}^2 - \beta_{13}^2 - \beta_{23}^2 \tag{20a}$$

$$\beta_{ij} = \Delta^2 \alpha_{ki}\alpha_{kj} \tag{20b}$$

$$\alpha_{ij} = \partial \tilde{u}_j / \partial x_i \tag{20c}$$

The tensor β is basically proportional to the gradient in conjuction with the gradient diffusion model (Clark *et al*., 1979). According to the previous work (Selle *et al*., 2007), the gradient diffusion model outperforms most other models for supercritical mixing layers. The model coefficient is used as c_v = 0.07. Compared with the most popular Smagorinsky model, Vremans's approach has the desirable feature that the SGS viscosity vanishes in the laminar flow.

2.5. Multi-environment PDF Model

The MEPDF approach in context with the conserved scalar approach has been adopted to numerically simulate the turbulent spray mixing processes under the transcritical and supercritical states. In the real-fluid spray jet, the mixture fraction is the most appropriate conserved scalar due to its applicability in the analysis of the non-premixed flames. The mixture fraction is defined as $Z = (Z_j - Z_{j,chamber})/(Z_{j,inlet} - Z_{j,chamber})$, where $Z_{j,inlet}$ and $Z_{j,chamber}$ indicate the mass fraction of element $_j$ in the nozzle stream.

The MEPDF method can be derived from the density-weighted transport equation for a one-point one-time joint composition PDF, f_ϕ (Fox, 2003; Kim *et al*., 2017):

$$\frac{\partial (f_\phi)}{\partial t} + \tilde{\mathbf{u}}\nabla\cdot(f_\phi) - \nabla\cdot(\Gamma_{eff}\nabla f_\phi) = -\frac{\partial}{\partial \psi_i}\left[\left(\Omega_m\left(\langle \phi_i \rangle - \psi_i\right) + S_i(\psi)\right) f_\phi\right] \tag{21}$$

Where the tilde denotes the Favre-averaged mean, $\boldsymbol{u}$ is the velocity vector, $\Gamma_{eff} = \mu/Sc + \mu_t/Sc_t$ is the effective diffusion coefficient. In this study, the micro mixing is represented by the interaction-by-exchange with the mean (IEM) model. In the present MEPDF approach, the PDF of the mixture fraction is approximated by two delta functions with different weights:

$$f_Z(Z;\mathbf{x},t) = \bar{\rho}\sum_{n=1}^{N_e} p_n(\mathbf{x},t)\delta\left[Z - Z_n(\mathbf{x},t)\right] \tag{22}$$

Where the bar denotes the Reynolds-averaged mean, ρ is the fluid density, N_e is the number of environments, $p_n(\boldsymbol{X}, t)$ is the mass weight of environment, and $Z_n(\boldsymbol{X}, t)$ is a mixture fraction of environment. The moment transport equation for the joint PDF is obtained by integrating the PDF transport equation in the composition space. One can derive the separated transported equations of weight and weighted abscissa for each environment with the zeroth and first moment transport equations of the PDF.

$$\frac{\partial(\bar{\rho}p_n)}{\partial t} + \frac{\partial}{\partial x_j}(\bar{\rho}\tilde{u}_j p_n) - \frac{\partial}{\partial x_j}\left(\Gamma_{eff}\frac{\partial p_n}{\partial x_j}\right) = a_n \tag{23}$$

$$\frac{\partial\left(\bar{\rho}\left[p_n Z_n\right]\right)}{\partial t} + \frac{\partial}{\partial x_j}\left(\bar{\rho}\tilde{u}_j\left[p_n Z_n\right]\right) - \frac{\partial}{\partial x_j}\left(\Gamma_{eff}\frac{\partial\left[p_n Z_n\right]}{\partial x_j}\right) = b_n + \bar{\rho}p_n\left(\Omega_m\left(\langle Z\rangle - Z_n\right)\right) \tag{24}$$

Here, a_n and b_n are additional source terms for preserving accuracy of high-order moment of mixture fraction. In this study, these terms are determined by the direct quadrature method of moment. The last term in Equation (23) representing the micro-mixing effect can be closed using IEM model. The mixing frequency, Ω_m is modeled in terms of mixing constant and turbulent time scale. The micro mixing constant value of 2.0 is used in the study.

The thermodynamic and transport properties were interpolated from the precomputed library to reduce the computational cost as well as to ensure numerical stability (Kim *et al*., 2012). The thermodynamic and transport properties used in the numerical analysis can be obtained with p_n and Z_n,

$$\tilde{\phi}(x,t) = \int_0^1 f(Z)\phi dZ \approx \sum \tilde{p}_n(\mathbf{x},t)\phi(Z_n) \tag{25}$$

The present reall-fluid MEPDF approach has been implemented into OpenFOAM (OF: www.openfoam.com) compressible flow solver which is based on the Pressure Implicit with Splitting of Operators (PISO) algorithm. To treat the pressure-velocity coupling in the real-fluid flows, the typical pressure equation needs to be properly modified for considering the non-idealities of EoS as well as for resolving the numerical instability due to the very stiff density gradient in the supercritical and transcritical region. In the real-fluid properties represented by the cubic EoS, the density is a function of pressure, enthalpy, and mass fraction. Thus, the density can be expressed by dividing three terms through the first-order Taylor expansion procedure (Müller *et al*., 2016). In the present study, the pressure equation is modified to realistically represent the real-fluid EoS by considering the effects of pressure, enthalpy, and mass fraction. This numerical procedure was validated in our previous studies (Kim *et al*., 2011, 2012)

involving a simulation of the cryogenic real-fluid mixing and combustion processes injection at supercritical pressures.

3. RESULTS AND DISCUSSION

The present real-fluid MEPDF approach has been applied to numerically investigate the physical processes of the non-reacting diesel-fueled spray jet under the supercritical pressure. As a validation case, we have chosen the non-reacting Spray-A among the benchmark target cases of the Engine Combustion Network. In the measurement (Pickett *et al*., 2011; Falgout *et al*., 2015), the pure liquid n-dedecane is injected from a injector nozzle with a diameter, 0.09 mm. The injection temperature and pressure are 363 K and 150 MPa, respectively. The chamber pressure is 60 bar and the mixture temperature is 900 K. In this non-reacting case, the ambient gaseous mixture consists of the large portion of nitrogen and the marginally smaller portion of CO_2 and H_2O. Since the temperature is nearly uniform in the chamber, the adiabatic wall condition is assumed for the simulation. The detailed operating conditions of this non-reacting spray A are summarized in Table 2. For n-dodecane fuel, the critical pressure is 18.1 bar and the critical temperature is 658.2 K. Therefore, in this chamber condition, the n-dodecane spray jet undergoes a transcritical process through the injection and turbulent mixing process with the ambient hot gaseous mixture.

The RANS calculations were performed in a two-dimensional axisymmetric region with a diameter of 60 mm and a height of 100 mm. The LES calculations used 750 M calculation cells in a three-dimensional region having a height of 20 mm and 80 mm in diameter. In order to minimize the numerical error, the computational grid is highly refined at the near injector region with the high gradient. In the experiments, n-dodecane was injected

Table 2. Operating condition for Spray-A non-reacting case.

Ambient temperature (K)	900	
Ambient pressure (MPa)	Near 6.0	
Ambient gas volume basis (%)	N_2	89.71
	CO_2	6.52
	H_2O	3.77
Vessel volume	1050d × 1080d	
Fuel	n-dodecane	
Fuel temperature (K)	363	
Fuel injection pressure (MPa)	150	
Duration time (ms)	1.5	
Total mass (mg)	3.5 ~ 3.7	
Nozzle diameter (mm)	0.09	

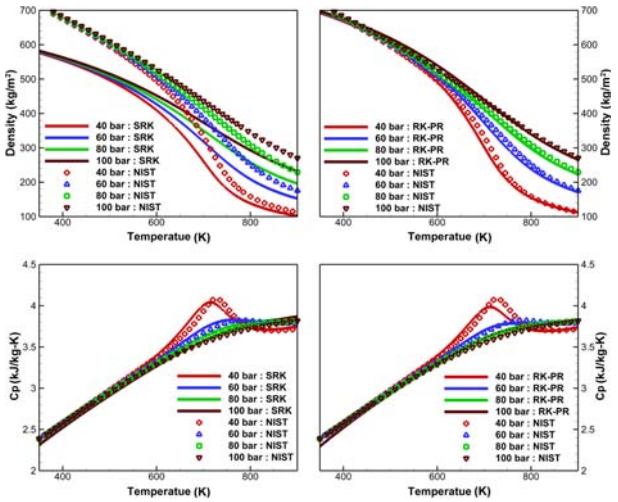

Figure 1. Density and isobaric specific heat of n-dodecane versus temperature for four pressures; comparison between NIST data and predictions by (a) SRK model and (b) RK-PR model.

during 6.0 ms and total injection mass was 11.73 mg. In the present simulation, the mass flow rate at the injector was specified by the temporally varying mass flow rate data provided by the ECN. In the mixture fraction domain, the boundary temperatures at fuel side and ambient side are 363 K and 900 K, respectively. The ambient mixture consists of 89.71 % N_2, 6.52 % CO_2, and 3.77 % H_2O in volume basis. With clustering at the high-gradient zone, the mixture fraction space is discretized by 101 bins. Before generating the real-fluid library, we have assessed the accuracy of two real-fluid equations of state including three-parameter RK-PR model and two-parameter SRK model by comparing with NIST data.

There are four pressure conditions compared to NIST data in Figure 1. At 40 bar, relatively close to the critical pressure (18.1 bar), this pseudo-boiling effect is more apparent. By increasing from 40 bar to 100 bar, the temperature at which pseudo-boiling occurs is increasingly higher, and thermodynamic properties are more smooth. As displayed in Figure 1, the three-parameter RK-PR model yields the much better conformity with NIST data while the two-parameter SRK model considerably underestimates the density level at the whole range of pressure and temperature. It can be seen that both of SRK and RK-PR model reasonably well predict the isobaric specific heat for the pressure range higher than 40 bar. However, at 40 bar closer to the critical state, there are the noticeable deviations with NIST data around the pseudo-boiling state. Especially at the operating pressure (60 bar), the RK-PR model yields the good conformity with NIST data in terms of density and isobaric specific heat. Thus, the present study has adopted the RK-PR EoS model to numerically simulate the real-fluid n-dodecane spray jet under the supercritical pressure.

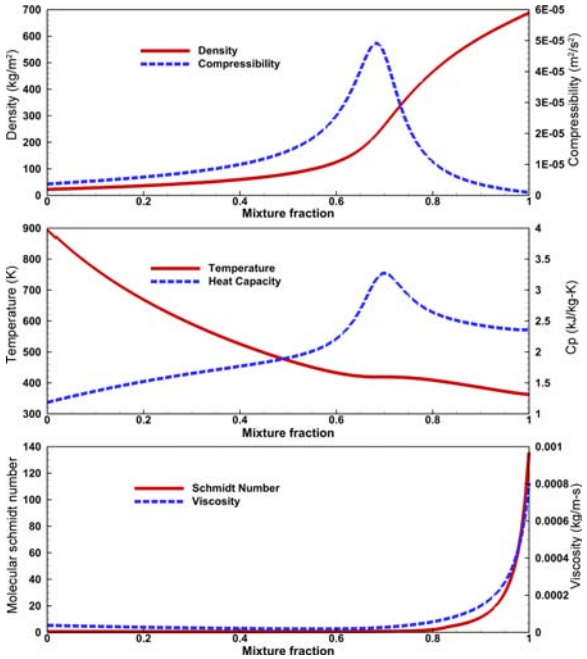

Figure 2. Density, compressibility, temperature, and isobaric specific heat, molecular Schmidt number, and viscosity in the real-fluid library in operating pressure (6 MPa).

Figure 2 shows the profiles of density, compressibility, temperature, and isobaric specific heat, molecular Schmidt number, and viscosity in the real-fluid library in operating pressure (6 MPa). It can be seen that thermodynamic properties are suddenly changed along the mixture fraction space. Especially there exist the strong non-linearities in thermophysical quantities. Unlike the cryogenic fluids including the liquid oxygen and liquid nitrogen (Kim *et al*., 2012), the non-cryogenic diesel fuels such as n-dodecane have the much higher viscosity and the much lower mass diffusity compared to the ambient gases. As illustrated in Figure 2, the corresponding molecular Schmidt number is remarkably high at the fuel-rich side. Thus, it is expected that the turbulence model might have additional difficulty to realistically predict the turbulent liquid-like high-density transcritical jet with the highly varying molecular Schmidt number.

Figure 3 shows the predicted and measured liquid and vapor penetration lengths versus the time up to 0.5 ms after injection. In the measurements, the vapor penetration length was determined from Schlieren imaging and the liquid penetration length was obtained from Mie scattering. The liquid and vapor penetration lengths are obtained from the simulation results using a threshold value of 0.6 and 0.01 for the fuel mass fraction, respectively. In this study, numerical results are obtained by RANS and LES based approach. In terms of the liquid and vapor penetration length, the LES-based model yields the overall conformity with measurement while the RANS-based model

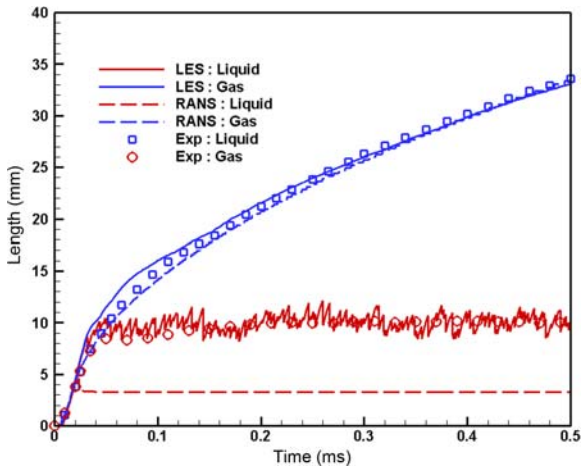

Figure 3. Predicted and measured liquid and vapor penetration lengths versus time up to 0.5 ms after injection.

unacceptably underestimates the penetration levels. The transient liquid penetration results obtained by the LES-based approach were close to experimental data temporally varying from 8 mm to 12 mm.

For a qualitative comparison of the injection sequence, numerical results are compared to the shadowgraphs of Pickett *et al*. (2011). In terms of the temporal sequence of the injection process, Figure 4 presents the comparison between experimental data and numerical results obtained by RANS and LES based turbulence model. In numerical results, the dark blue region is corresponding to the liquid core where the mixture fraction is larger than 0.6. As shown in Figure 4, in terms of liquid spray penetration trends, the LES-based model yields the qualitatively overall agreement with the measured image, while the RANS-based model underestimates the penetration level unrealistically. However, in terms of gas penetration trends, numerical results obtained by both models are the reasonably good agreement with experimental data. With a closer look at the near-injector region, it is found that the present LES-based approach noticeably underestimates the spreading angle of the injected fuel jet and this trend is directly tied with the overestimated liquid penetration at the earlier stage. The similar tendency was reported in the previous LES-based studies (Ruiz *et al*., 2015; Ma and Ihme, 2017). These results suggest that the present real-fluid approach has the limitations to realistically represent the near-injector interfacial multi-phase flows which might accompany with liquid disintegration and turbulence-droplet interaction. The previous experimental studies on supercritical turbulent jets (Oschwald *et al*., 2006) show that the larger injectant-to-chamber density ratio yields the longer jet potential core. Thus, the strong density gradients result in stabilization effect on hydrodynamic instabilities. In the upstream region, LES results indicate that the high-speed liquid-like density jet maintains the self-similar behavior roughly up to the relatively long distance prior to

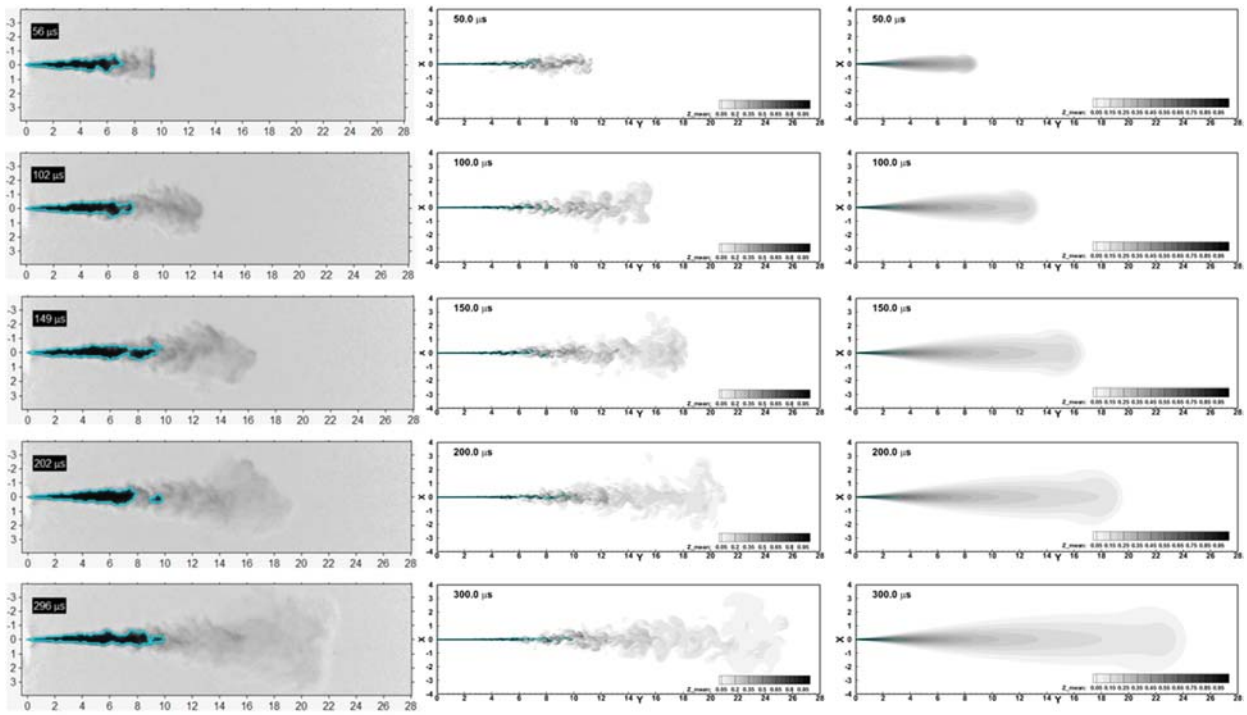

Figure 4. Comparison between measurement and prediction for temporal sequence of the injection process.

the disintegration of the central dense core.

Figure 5 shows the predicted contours of time-averaged axial velocity, mixture fraction, temperature, density, isobaric specific heat, and isoenthalpic compressibility in the high-pressure n-dodecane spray jet. In these predicted real-fluid spray fields, the black bold line corresponding to the mixture fraction 0.6 is regarded as the boundary line between the inner liquid-fuel core and the fuel vapor. Due to the pseudo-boiling effect at the region near this boundary line in the inner core region, the isobaric specific heat remarkably increases and the cold core liquid n-dodecane jet is abruptly expanded. In this pseudo-boiling region, heat transfer to the liquid fuel does not noticeably increase its temperature, but merely increases its specific volume. Therefore, the density decreases sharply in this region, and the temperature variation is marginally small. As displayed in Figure 5, the RANS-based model and the LES-based approach predict the distinctly different turbulent mixing field in the transcritical near-injector region.

The RANS-based approach greatly overestimates the turbulent diffusion and mixing in the near-injector liquid core region and the resulting pseudo-boiling processs fastly occurs. Thus, the corresponding liquid penetration lengths are unrealistically underestimated.

This discrepancy could be attributed to the inherent shortcomings of the RANS-based turbulence model with the gradient diffusion approach adopted for modeling the scalar-velocity correlation. Moreover, it is necessary to note that the semi-empirical model constants were optimized for the simulation of subcritical turbulent gaseous jets. Thus, the RANS model has the tendency to overestimate the turbulent diffusion in the turbulent liquid-like high-density transcritical jet with the highly varying molecular Schmidt number. On the other hand, in the LES simulations, the scalar transport process is dominantly controlled by the large-scale turbulence resolved in the numerical grid while the sub-grid turbulent diffusivity is quite low. Thus, compared to the RANS model, the LES approach realistically predicts the turbulent diffusion and the pseudo-boiling processs especially in the transcritical near-injector region.

Consequently, the LES-based MEPDF approach yields the much better conformity with experimental data in terms of spray penetration length and vapor penetration length. Thus, these results imply that the LES-based MEPDF approach has the capability to realistically predict the turbulent mixing processes of the transcritical n-dodecane turbulent jet.

Figure 6 shows the predicted and measured centerline profiles of mean and rms mixture fraction, mean temperature. At the relatively downstream regions ($x > 16$ mm), the present study has made the comparison between numerical results and experimental data obtained by Rayleigh scattering. At the axial locations ($x > 18$ mm) apart from the injector, numerical results obtained by two turbulent models are in good agreement with the measured profiles in terms of mean and rms mixture fraction, and

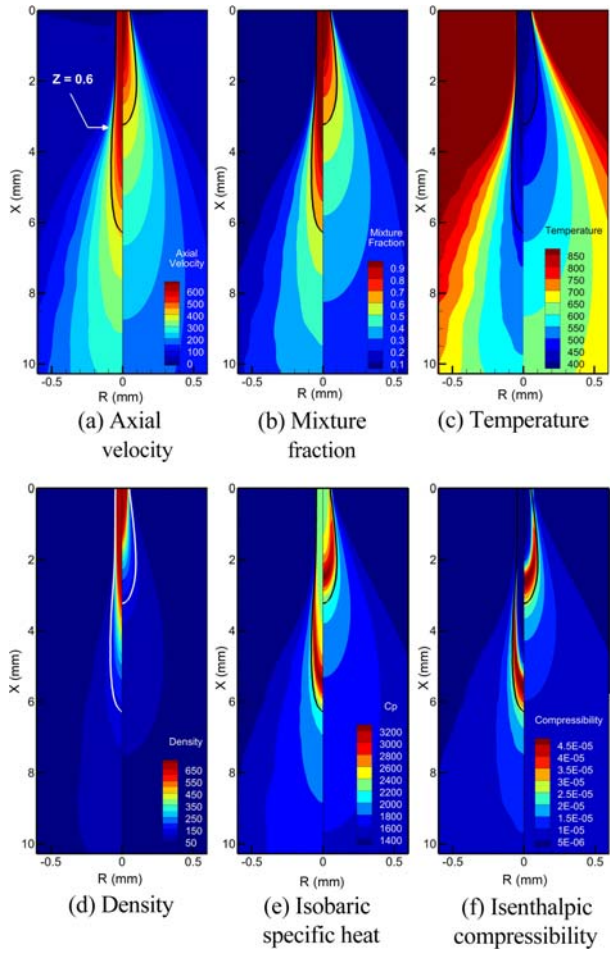

Figure 5. Predicted contours of time-averaged axial velocity, mixture fraction, temperature, density, isobaric specific heat, and isoenthalpic compressibility.

mean temperature. However, in a relatively upstream region (x < 12 mm) where a transcritical mixing process occurs, the LES-based approach predict much slower mixing process and much longer intact core while the RANS-based model predict much faster mixing and much shorter intact core. LES results reveal that the peak mixture fraction is maintained up to the axial location (x = 2.5 mm) and then it is sharply decayed. On the other hand, RANS results indicate that the mixture fraction field is rapidly decayed at the near-injector locaation (x = 0.6 mm). Two predicted profiles are merged to the nearly identical level in the proximity with the axial station (x = 18 mm). The LES-based approach also yields the much sharper gradient in the decay zone of the mixture fraction and the much higher peak level of the mixture fraction variance, compared to the RANS-based model. It is necessary to note that the sharp decay zone of the mixture fraction is corresponding to the region where the pseudo-boiling mostly occurs.

Figure 7 shows the expected radius profiles for the mean and rms mixture fractions at relatively upstream locations

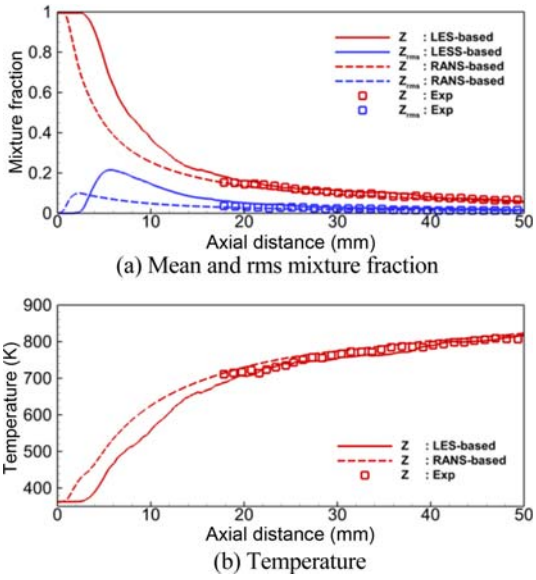

Figure 6. Predicted and measured centerline profiles of mean/rms mixture fraction and mean temperature.

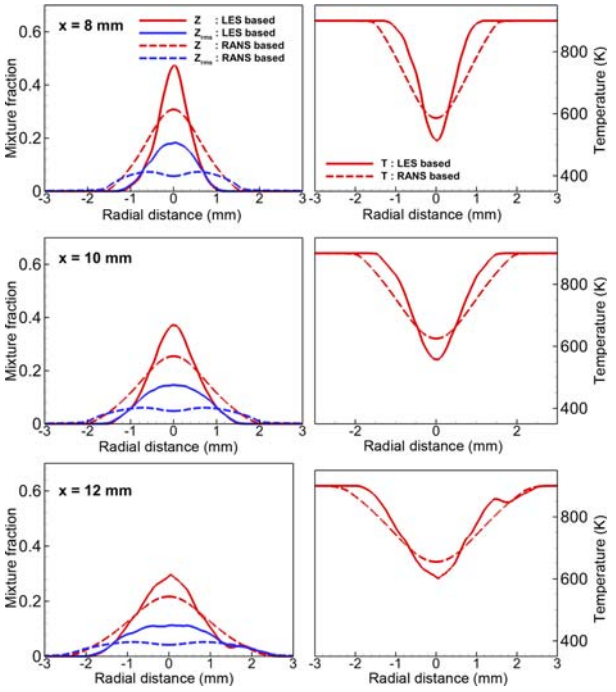

Figure 7. Predicted and measured radial profiles of the mean/rms mixture fraction and mean temperature at the relatively upstream locations (x = 8, 10, and 12 mm).

(x = 8, 10, 12 mm) where physical processes including auto-ignition and flame stabilization occurs in case of the reacting spray jets. The LES-based approach predicts the much higher peak levels in the mixture fraction and its variance, compared to the RANS-based model. This tendency becomes progressively apparent at the more upstream region (x = 8 mm).

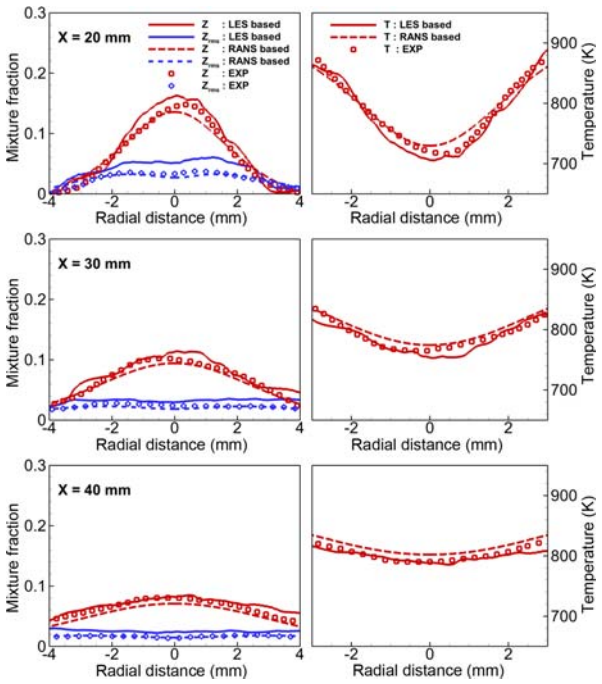

Figure 8. Predicted and measured radial profiles of the mean/rms mixture fraction and mean temperature at the relatively downstream locations (x = 20, 30, and 40 mm).

As shown in Figures 6 and 7, the RANS-based model yields the much faster axial decay rate and the much higher radial spreading in this upstream region than does the LES-based approach.

Figure 8 presents the predicted and measured radial profiles of mean/rms mixture fraction and mean temperature at the relatively downstream locations (x = 20, 30 and 40 mm). It can be seen that two approaches (RANS, LES) yield the reasonably agreement with experimental data in terms of mean/rms mixture fraction and mean temperature even if LES-based model marginally overestimates the mixture fraction and its variance. However, in the upstream region (x < 20 mm) with the crucial physical processes including autoignition and flame stabilization, the present numerical results clearly indicate that the LES-based MEPDF approach has the much better prediction capability for the turbulent mixing processes of the noncryogenic n-dodecane turbulent jet under the supercritical pressure.

4. CONCLUSION

The multi-environment probability density function approach using the real-fluid EoS has been developed to numerically investigate the physical processes of the non-cryogenic n-dodecane fuel spray jet under the supercritical pressure. The detailed discussions are made for the prediction capability of RANS/LES based real-fluid approach as well as the essential features of the real-fluid n-dodecane jet under the supercritical pressure. Based on the results, the following conclusion can be drawn.

(1) In terms of the liquid and vapor penetration length, the LES-based model yields the overall conformity with measurement while the RANS-based model unacceptably underestimates the penetration levels.
(2) It was found that the strong density gradients in the supercritical n-dodecane jet lead to delay the destabilization of the jet in the upstream region. Thus, the strong density gradients result in stabilization effect on hydrodynamic instabilities.
(3) Due to the shortcomings of the gradient diffusion model, the RANS-based approach greatly overstimates the turbulent diffusion and mixing in the near-injector liquid core region and the resulting pseudo-boiling processs fastly occurs. Unlike the RANS-based model, the LES-based approach realistically predicts the turbulent diffusion and the pseudo-boiling processs especially in the transcritical near-injector region.
(4) The LES-based MEPDF approach yields the much better conformity with experimental data in terms of spray penetration length and vapor penetration length. Thus, these results imply that the LES-based MEPDF approach has the capability to realistically predict the turbulent mixing processes of the transcritical n-dodecane turbulent jet.
(5) At the relatively downstream locations (x > = 20 mm), two approaches (RANS, LES) yield the reasonable agreements with experimental data in terms of mean/rms mixture fraction and mean temperature. In the upstream region (x < 20 mm) with the crucial physical processes including autoignition and flame stabilization in reacting case, the present numerical results clearly indicate that the LES-based MEPDF approach will show better predictive ability than RANS-based MEPDF approach for the turbulent mixing processes of the non-cryogenic n-dodecane turbulent jet under the supercritical pressure.

ACKNOWLEDGEMENT–This work was supported by the Development of 300 MW class Korean IGCC demonstration plant technology of the Korea institute of Energy Technology Evaluation and Planning (KETEP) grant funded by the Korea government Ministry of Knowledge Economy.

REFERENCES

Chung, T. H., Ajlan, M., Lee, L. L. and Starling, K. E. (1988). Generalized multiparameter correlation for nonpolar and polar fluid transport properties. *Industrial and Engineering Chemistry Research* **27**, **4**, 671–679.

Cismondi, M. and Mollerup, J. (2005). Development and application of a three-parameter RK–PR equation of state. *Fluid Phase Equilibria* **232**, **1-2**, 74–89.

Clark, R. A., Ferziger, J. H. and Reynolds, W. C. (1979). Evaluation of subgrid-scale models using an accurately

simulated turbulent flow. *J. Fluid Mechanics* **91**, **1**, 1–16.

Coklja, D., Kim, S. E., Iaccarino, G. and Drubin, P. A. (2003). A comparative assessment of the V2F model for recirculating flows. *Proc. 41st Aerospace Sciences Meeting and Exhibition*, Reno, Nevada, USA.

Congiunti, A., Bruno, C. and Giacomazzi, E. (2003). Supercritical combustion properties. *Proc. 41st Aerospace Sciences Meeting and Exhibition*, Reno, Nevada, USA.

Durbin, P. A. (1995). Separated flow computations with the κ-ε-v^2 model. *AIAA J.* **33**, **4**, 659–664.

ECN (2015). https://ecn.sandia.gov

Falgout, Z., Rahm, M., Wang, Z. and Linne, M. (2015). Evidence for supercritical mixing layers in the ECN Spray A. *Proc. Combustion Institute* **35**, **2**, 1579–1586.

Fox, R. O. (2003). *Computational Models for Turbulent Reacting Flows*. Cambridge University Press. Cambridge, UK.

Grisch, F., Bouchardy, P. and Clauss, W. (2003). CARS thermometry in high pressure rocket combustors. *Aerospace Science and Technology* **7**, **4**, 317–330.

Gurliat, O., Schmidt, V., Haidn, O. J. and Oschwalda, M. (2003). Ignition of cryogenic H_2/LOX sprays. *J. Aerospace Science and Technology* **7**, **7**, 517–531.

Kim, D., Stoesser, T. and Kim, J. H. (2013). The effect of baffle spacing on hydrodynamics and solute transport in serpentine contact tanks. *J. Hydraulic Research* **51**, **5**, 558–568.

Kim, H. J., Kang, S. M., Kim, Y., Lee, J. H. and Lee, J. K. (2006). Transient flamelet modeling for combustion processes of HSDI diesel engines. *Int. J. Automotive Technology* **7**, **2**, 129–137.

Kim, N. S. and Kim, Y. M. (2017). Multi-environment probability density function approach for turbulent partially-premixed methane/air flame with inhomogeneous inlets. *Combustion and Flame*, **182**, 190–205.

Kim, N., Jung, K. and Kim, Y. (2018). Multi-environment PDF modeling for n-dodecane spray combustion processes using tabulated chemistry. *Combustion and Flame*, **192**, 205–220.

Kim, S.-K., Choi, H.-S. and Kim, Y. (2012). Thermodynamic modeling based on a generalized cubic equation of state for kerosend/LOx rocket combustion. *Combustion and Flame* **159**, **3**, 1351–1365.

Kim, T. H., Kim, Y. M. and Kim, S. K. (2011). Numerical study of cryogenic liquid nitrogen jets at supercritical pressures. *J. Supercritical Fluids* **56**, **2**, 152–163.

Ma, P. C. and Ihme, M. (2017). Modeling and simulation of diesel injection at transcritical conditions. *Proc. ILASS-Americas 29th Annual Conf. Liquid Atomization and Spray Systems*, Atlanta, Georgia, USA.

Müller, H., Niedermeier, C. A., Matheis, J., Pfitzner, M. and Hickel, S. (2016). Large-eddy simulation of nitrogen injection at trans- and supercritical conditions. *Physics of Fluids*, **28**, 015102.

Oschwald, M., Smith, J. J., Branam, R., Hussong, J., Shick, A., Chehroudi, B. and Talley, D. (2006). Injection of fluids into supercritical environments. *Combustion Science and Technology* **178**, **1-3**, 49–100.

Pei, Y., Hawkes, E. R., Kook, S. H., Goldin, G. M. and Lu, T. (2015). Modelling n-dodecane spray and combustion with the transported probability density function method. *Combustion and Flame* **162**, **5**, 2006–2019.

Peng, D. and Robinson, D. B. (1976). A new two-constant equation of state. *Industrial and Engineering Chemical Fundamental* **15**, **1**, 59–64.

Pickett, L. M., Genzale, C. L., Manin, J., Malbec, L. M. and Hermant, L. (2011). Measurement uncertainty of liquid penetration in evaporating diesel spray. *Proc. 23rd Annual Conf. Liquid Atomization and Spray Systems*, Ventura, California, USA.

Ruiz, A., Lacaze, G., Misdariis, A. and Oefelein, J. C. (2015). Analysis of high-pressure diesel fuel injection processes using LES with real-fluid thermodynamics and transport. *Proc. Combustion Institute* **35**, **2**, 1603–1611.

Selle, L. C., Okong'o, N. A., Bellan, J. and Harstad, K. G. (2007). Modelling ofsubgrid-scale phenomena in supercritical transitional mixing layers: An a priori study. *J. Fluid Mechanics*, **593**, 57–91.

Soave, G. (1972). Equilibrium constants from a modified Redlich-Kwong equation of state. *Chemical Engineering Science* **27**, **6**, 1197–1203.

Takahashi, S. (1975). Preparation of a generalized chart for the diffusion coefficient of gases at high pressure. *J. Chemical Engineering of Japan* **7**, **6**, 417–420.

Vreman, W. (2004). An eddy-viscosity subgrid-scale model for turbulent shear flow: Algebraic theory and applications. *Physics of Fluids* **16**, **10**, 3670–3681.

Wehrfritz, A., Kaario, O., Vuorinen, V. and Somers, B. (2016). Large eddy simulation of n-dodecane spray flames using flamelet generated manifolds. *Combustion and Flame*, **167**, 113–131.

Wu, X. and Durbin, P. A. (1999). Numerical simulation of heat transfer in a transitional boundary layer with passing wakes. *J. Heat Transfer* **122**, **2**, 248–257.